catalysts

MDPI

Article

Regulating the Hydrodeoxygenation Activity of Molybdenum Carbide with Different Diamines as Carbon Sources

Linyuan Zhou [1], Huiru Yang [1], Xiangze Du [2] and Changwei Hu [1,*]

[1] Key Laboratory of Green Chemistry and Technology, Ministry of Education, College of Chemistry, Sichuan University, Chengdu 610064, China; zhoulinyuan1999@163.com (L.Z.); 202132203066@stu.scu.edu.cn (H.Y.)
[2] State Key Laboratory of Catalysis, Dalian Institute of Chemical Physics, Chinese Academy of Sciences, Dalian 116023, China; xiangzedu@dicp.ac.cn
* Correspondence: changweihu@scu.edu.cn; Tel.: +86-028-8541-1105

Abstract: The hydrodeoxygenation (HDO) of renewable fats or fatty acids into alkanes is a powerful measure to address energy and environmental crises. Molybdenum carbide-based catalysts are promising due to their platinum-like noble metal electronic properties. In this paper, Mo_2C catalysts were prepared by one-step carbonization of amine molybdenum oxide (AMO) precursors using diamines with different carbon chain lengths as ligands. The physical and chemical properties and the HDO catalytic activity of the catalysts were investigated. The results indicate that as the carbon chain of diamines in the precursor increases, the carbon content of the catalysts in the surface and bulk phase increases. The Mo_2C-12 catalyst exhibited excellent catalytic performance, with a palmitic acid conversion rate of 100% and an alkane selectivity of 96.6%, which are attributed to the smallest particle size, largest pore size, and synergistic effect of carbon. This work provides a simple and safe method for regulating the surface properties of Mo_2C catalysts.

Keywords: hydrodeoxygenation; Mo_2C catalyst; palmitic acid; alkanes

Citation: Zhou, L.; Yang, H.; Du, X.; Hu, C. Regulating the Hydrodeoxygenation Activity of Molybdenum Carbide with Different Diamines as Carbon Sources. *Catalysts* **2024**, *14*, 138. https://doi.org/10.3390/catal14020138

Academic Editor: Inés Moreno García

Received: 13 January 2024
Revised: 2 February 2024
Accepted: 8 February 2024
Published: 10 February 2024

1. Introduction

The production of energy and chemicals from non-renewable fossil resources has resulted in substantial pollution, which has brought about a series of negative impacts on the climate and the environment. Therefore, it is urgent to develop alternative energy that is clean and sustainable [1–3]. Clean electrical energy has achieved much progress in the renewable energy field [4–6]. However, due to the high energy density of hydrocarbon fuels, they are still temporarily difficult to be replaced in heavy transportation, agriculture, and other fields. Faced with these challenges, biomass resource, as a type of promising and ideal energy, is expected to obtain biofuels with a low CO_2 footprint. As the CO_2 generated during the combustion of biofuels comes entirely from the CO_2 captured by organisms from the atmosphere, thus biofuels are considered carbon neutral [7,8].

Hydrocarbon fuels can be produced from the hydrodeoxygenation of fatty acids and fatty acid esters that are derived from biomass, which has been receiving widespread attention from researchers recently [9–11]. Benefiting from their excellent activity, precious metal catalysts are widely used to produce diesel-like hydrocarbons from bio oils and bio fats, such as Pt [12], Pd [13], and Ru [14]. However, the high cost and rare reserves of these precious metals have deterred their widespread use. Molybdenum carbides represent a higher density of states near the Fermi level owing to the incorporation of carbon atoms at the interstitial sites of Mo, which imparts both the electron configuration and catalytic behaviors similar to that of noble metals [15]. In view of this, molybdenum carbide catalysts exhibit excellent activity in many reactions [16–19]. However, molybdenum carbides are usually synthesized by temperature-programmed reduction (TPRe) of molybdenum oxide under an atmosphere containing CH_4 or other hydrocarbons [20]. Since CH_4 used for carbonization is often flowing and excessive, several drawbacks have been brought out. On the

one hand, the use of mixed combustible gases increases the risk of experiments; on the other hand, this will result in excessive hydrocarbon gases emitted into the atmosphere. In fact, methane has a more severe greenhouse effect than CO_2 [21], which goes against the original intention of alleviating energy and environmental problems. Hence, new methods to synthesize molybdenum carbides without CH_4 or other types of hydrocarbon gases should be developed. The carbonization of organic–inorganic hybrids to obtain molybdenum carbides can avoid the use of methane. Deng et al. [22] prepared an N-doped Mo_2C-embedded porous carbon network (Mo_2C@PCN) using chitosan as a carbon source, which showed excellent performance as a cathode catalyst for lithium–sulfur batteries. Wan et al. [23,24] found that four crystal phases of molybdenum carbides could be obtained by carbonization of amine–metal oxide (AMO) composites. The hydrogen evolution reaction (HER) activities of these catalysts with four phases have been explored. They also investigated the effects of different amines, promoters, and synthesis conditions on morphology and crystal phases. Lin et al. [25] synthesized MoC-Mo_2C heteronanowires successfully through controlled carbonization of AMO, which achieved efficient HER. A large number of studies have shown that the ratio of amines and carbonization temperature are key factors in controlling the crystal phase ratio. Molybdenum carbide catalysts can be obtained from organic–inorganic hybrid precursors, and the surface properties of these catalysts can be adjusted by changing the type of carbon resources, preparation conditions, and carbonization process. However, further research is needed to reveal the formation process of carbides and the influence of different surface properties on hydrodeoxygenation activity.

Herein, different AMO precursors were synthesized using diamines with different carbon chain lengths. Through a one-step carbonization method, Mo_2C catalysts with different carbon contents were subsequently obtained. The evolution of the AMO precursors to molybdenum carbides and the influence of residual carbon on the surface structure and properties of the catalysts were investigated. Moreover, the hydrodeoxygenation performance of these catalysts has been further evaluated for the conversion of palmitic acid.

2. Results and Discussion

2.1. Characterizations of Catalyst

2.1.1. XRD Results

XRD was used to characterize the crystal phase and crystallite sizes of both precursors and catalysts prepared using different diamines as carbon sources for carbonization. As is presented in Figure 1a, the XRD patterns of different precursors show different diffraction peaks. The diffraction peaks with the strongest intensity of these precursors are located at $2\theta = 9.6°$, 7.3°,6.4°, and 5.4°. When the carbon number of diamines increases, the volume of unit cells in the formed AMO precursors also increases, which leads to wider interplanar spacing. Therefore, the peaks located at the lowest 2θ degree shift towards a smaller angle from AMO-6 to AMO-12. All patterns are attributed to the AMO generated by the corresponding diamine, as no diffraction peak of molybdenum oxides is found. The XRD pattern of AMO-6 is consistent with $(NH_3C_6H_{12}NH_3)\cdot Mo_3O_{10}$ (PDF#00-058-1680), while the XRD pattern of AMO-8 is attributed to $(NH_3C_8H_{16}NH_3)_2\cdot Mo_8O_{26}$ (PDF#00-058-1315). Even though AMO-10 and AMO-12 cannot be attributed to any PDF card (PDF 5+, 2024), it can be anticipated that all the precursors prepared with different diamines formed AMO. Based on elemental analysis and TG results shown in Figure S1 and Table S1, the chemical formula of the precursor was calculated. The simplest chemical compositions of AMO-10 and AMO-12 are $(NH_3C_{10}H_{20}NH_3)\cdot Mo_4O_{13}$ and $(NH_3C_{12}H_{24}NH_3)\cdot Mo_4O_{13}$. As shown in Figure 1b, all the catalysts show similar XRD patterns, and the characteristic diffraction peaks located at $2\theta = 34.4°$, 38.0°, 39.4°, 52.1°, 61.5°, 69.6°, 72.4°, 74.6°, and 75.5° are ascribed to β-Mo_2C (PDF#00-035-078). The average crystallite sizes of Mo_2C were calculated by the Scherrer equation using the strongest peak located at $2\theta = 39.4°$ [26]. The average crystallite sizes of Mo_2C were 17.4, 14.5, 13.9, and 11.7 nm of Mo_2C-6, Mo_2C-8, Mo_2C-10, and Mo_2C-12, respectively, which display a decreased trend with the increase in carbon numbers in the used diamine. The Mo_2C-12 prepared by 1,12-diaminododecane exhibits

the smallest crystallite size for Mo_2C. It implied that, under the present carbonization condition, the crystallite size can be adjusted by changing the carbon chain length of the diamine in AMO precursors. This might be owing to the larger spacing between unit cells in the AMO-12 crystal, which prevents carbides from agglomerating into larger sizes at high temperatures.

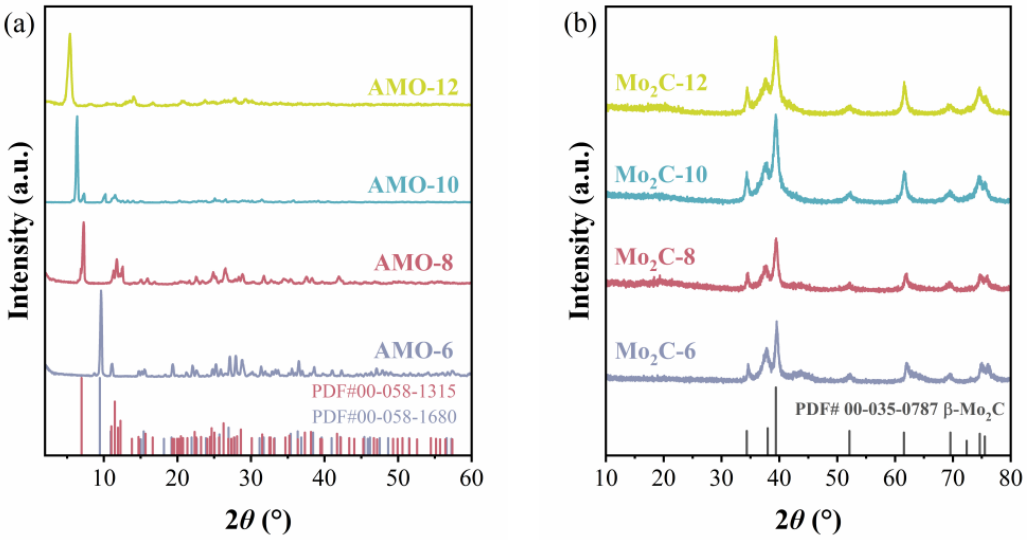

Figure 1. XRD patterns of (**a**) different amine–metal oxide composite precursors and (**b**) catalysts prepared with different diamines carbonized at 700 °C.

2.1.2. TGA-DSC Results

In order to investigate the formation of Mo_2C during the carbonization procedure, TGA-DSC of AMO precursors under Ar atmosphere was conducted. It can be observed in Figure 2 that all the precursors exhibit two stages of weight loss with increasing temperature. The first weight loss stage occurs between 250 and 450 °C, and the second one occurs between 600 and 720 °C. Mo_2C was obtained from the carbonization of precursors, and the weight loss rates were 43.0%, 44.7%, 45.5%, and 47.5% for AMO-6, AMO-8, AMO-10, and AMO-12, respectively. The DSC curve indicates that self-carbonization is an endothermic process when generating these catalysts, which is evident near 270 °C and 700 °C. To further clarify the forming process of β-Mo_2C from AMO, treatments for AMO-12 under different temperatures (275 °C, 400 °C, 500 °C, and 600 °C) were conducted, and the obtained samples were subsequently characterized by XRD. The corresponding results are shown in Figure 3. When carbonized at 275 °C, the flat broad peak at 21.5° is attributed to amorphous carbon. The endotherm peak of the DSC curve at 273 °C may be due to the disruption of the interaction between the diamine and Mo_xO_y clusters [27], followed by the formation of carbonized species. As the temperature increases, the intensity of the characteristic peak (5.4°) of AMO-12 gradually weakens, while the peaks of α-MoC_{1-x} gradually strengthen. However, the crystallinity of α-MoC_{1-x} is very poor. When carbonized at 700 °C, β-Mo_2C eventually generated. Neither MoO_2 nor MoO_3 is observed during the carbonization process of AMO-12, indicating that molybdenum carbide is directly generated from the organic–inorganic hybrid precursor and further underwent a phase-transition process converting α-phase to β-phase. The peaks of the DSC curve at 680 °C and 708 °C are attributed to phase transformation and crystallization, which are also important endothermic processes. The differences in endothermic effects between various AMO precursors are probably caused by different interaction of the diamines and Mo_xO_y clusters, for example, hydrogen bonding [28–30] or electrostatic interaction [31], as well as the intensity of these interactions.

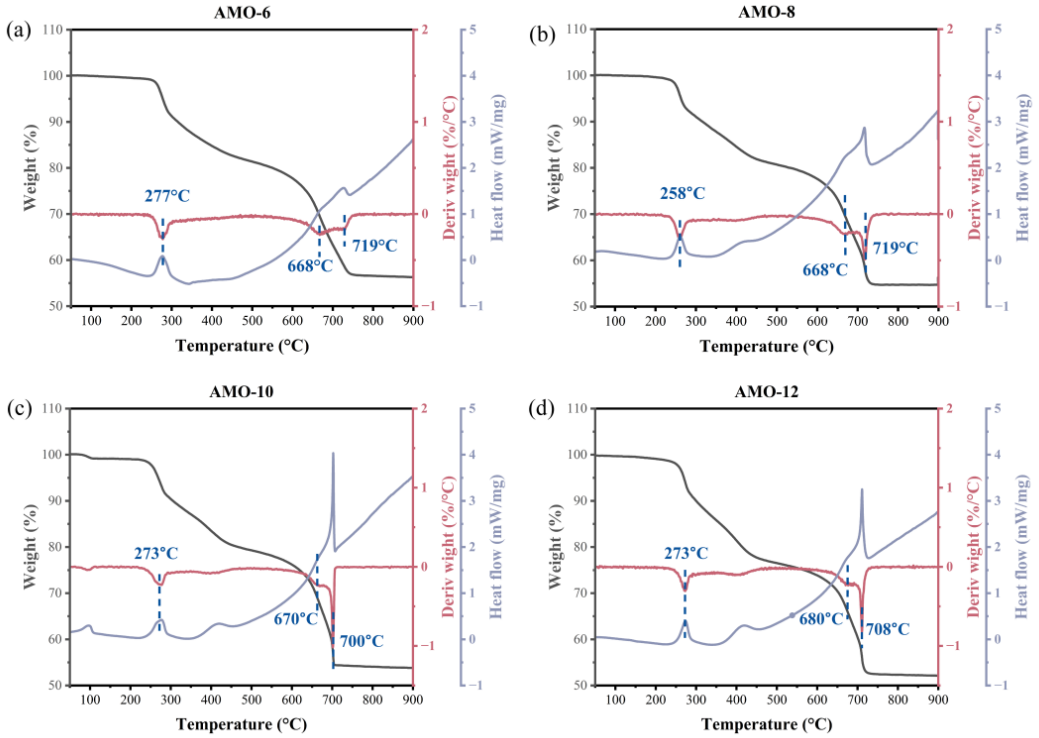

Figure 2. TGA/DTG/DSC curves for AMO precursors with different diamines: (**a**) 1,6-Hexanediamine; (**b**) 1,8-Diaminooctane; (**c**) 1,10-Diaminodecane; (**d**) 1,12-Diaminododecane.

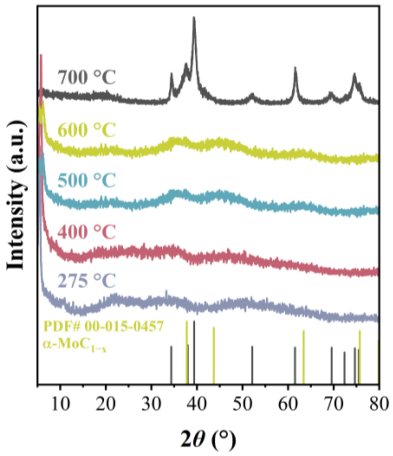

Figure 3. XRD patterns of AMO-12 heated at different temperatures.

2.1.3. SEM, TEM, and HRTEM Results

The morphology and structural characteristics of catalysts were revealed by SEM and TEM. The SEM images of both precursors and catalysts are shown in Figure 4. There are no significant differences in the morphologies of precursors and catalysts. It indicates that organic amines can indeed serve as soft templates for controlling the morphology of molybdenum carbide, thus the catalyst morphology remains unchanged after carbonization [24]. Among them, AMO-6 and Mo_2C-6 appear in granular form, while AMO-8 and Mo_2C-8 are mainly presented in the rod-shaped form of stacked nanosheets, accompanied with some fragmented sheet-like structures. The other catalysts and precursors (AMO-10, AMO-12, Mo_2C-10, and Mo_2C-12) exhibit irregular nanosheet morphology. Unlike AMO-8, these nanosheets are not further stacked to form the higher-level structures. It is worth noting that there is a layer of amorphous carbon (circled in red) coated on the surface of Mo_2C-10 and Mo_2C-12, which may be formed by the excessive carbon during the carbonization

process since the used diamines are with more carbon atoms. Moreover, HRTEM images show that the lattice fringes with distances of 0.24 and 0.23 nm appear on all catalysts, corresponding to the (0 0 2) and (1 0 1) crystal planes of β-Mo_2C, respectively. This result is consistent with that of XRD, i.e., all the catalysts are presented with β-Mo_2C, even using different amines as carbon resources.

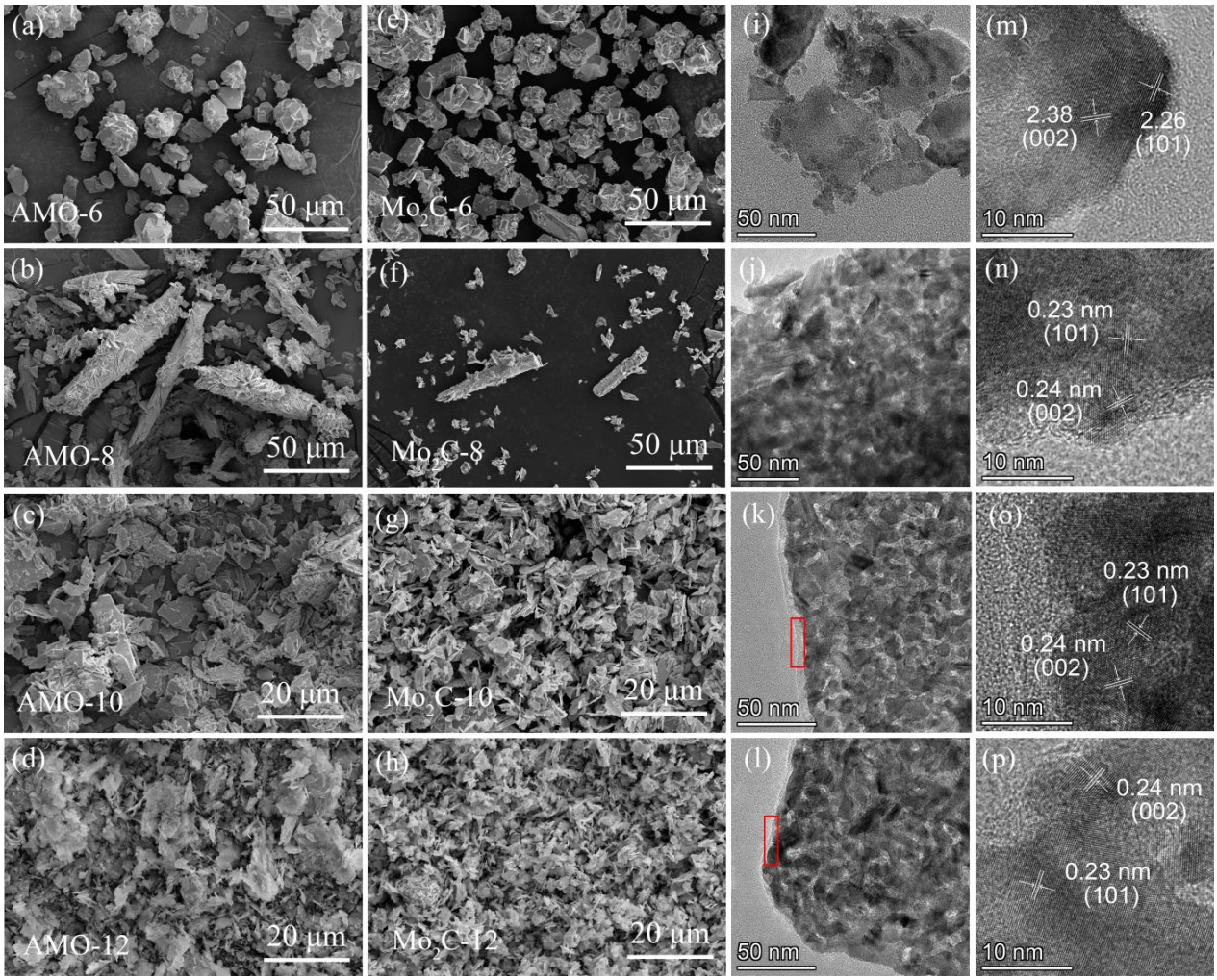

Figure 4. SEM images of AMO precursors (**a**–**d**) and catalysts (**e**–**h**). TEM images of (**i**) Mo_2C-6; (**j**) Mo_2C-8; (**k**) Mo_2C-10; (**l**) Mo_2C-12. HRTEM images of (**m**) Mo_2C-6; (**n**) Mo_2C-8; (**o**) Mo_2C-10; (**p**) Mo_2C-12.

2.1.4. BET and BJH Results

To explore the textural properties of various catalysts, N_2 adsorption–desorption isotherms were measured, and the corresponding results are shown in Figure 5 and Table 1. As shown in Figure 5a, all the catalysts display IV-type nitrogen adsorption–desorption isotherms with evident H4 hysteresis loops at relative pressures of 0.4–1.0, indicating that the catalysts have irregular mesoporous structures. This is also evident in the pore size distribution curves shown in Figure 5b. Although the different diamines used have no significant effect on the formed crystal phase, they display a significant impact on the pore structure of the catalysts. With the increase in carbon number in the used diamine, the specific surface area of the catalyst decreases, while the pore size increases. This indicates that when the used diamine has a shorter carbon chain, it tends to generate more pores with small sizes, thus leading to a larger specific surface area. When 1,12-diaminododecane is used as the carbon source, the Mo_2C-12 displays the smallest specific surface area (31.4 m^2/g) and the largest average pore size (14.7 nm).

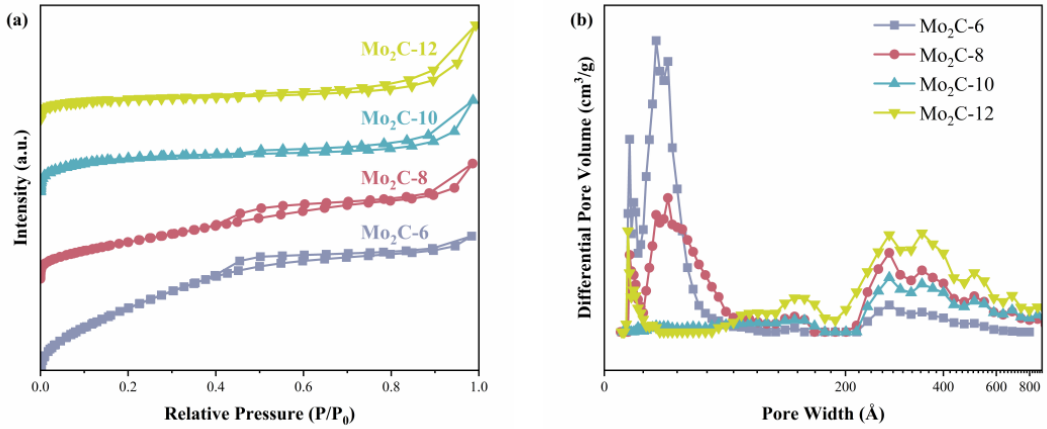

Figure 5. (**a**) Nitrogen adsorption–desorption isotherms and (**b**) BJH pore-size distribution curves of different catalysts.

Table 1. Textural properties and element contents of catalysts.

Catalyst	S_{BET} [a] (m_2/g)	V_{BJH} [b] (cm^3/g)	D_P [c] (nm)	Mo [d] (wt%)	C [e] (wt%)	N [e] (wt%)	Mo/C [f]
Mo_2C-6	90	0.062	3.1	79.0	6.6	0.2	1.5
Mo_2C-8	57	0.058	4.4	82.7	7.2	0.2	1.4
Mo_2C-10	53	0.035	7.5	77.1	9.3	0.2	1.0
Mo_2C-12	31	0.039	14.7	78.1	9.5	0.2	1.0

[a] Surface area (S_{BET}) determined by the BET method; [b] BJH adsorption cumulative volume of pores; [c] BJH adsorption average pore diameter; [d] Obtained by ICP, weight percentage content; [e] Obtained by elemental analysis, weight percentage content; [f] Atomic ratio.

As listed in Table 1, the content of Mo in different catalysts was tested by ICP, while the content of C and N was obtained by elemental analysis. The carbon content of Mo_2C-6, Mo_2C-8, Mo_2C-10, and Mo_2C-12 was 6.6%, 7.2%, 9.3%, and 9.5%, respectively, which gradually increases with the longer carbon chain length of diamines used for precursors preparation. The C/Mo atomic ratios were further calculated, and all of them were <2, indicating that there are other types of carbon presented besides β-Mo_2C. Combined with the XRD results displayed in Figure 3, it is reasonable to conclude that α-MoC_{1-x} is first generated and undergoes a phase transition at sustained high temperatures, ultimately resulting in the formation of β-Mo_2C and C.

2.1.5. XPS Result

The surface element compositions and chemical states of the Mo_2C catalysts were characterized by XPS experiments, and the obtained results are shown in Figure 6. Four pairs of peaks were deconvoluted in the spectrum of high-resolution Mo 3d spectroscopy. The peaks near 228.3 eV are referred to Mo $3d_{5/2}$ and corresponded to Mo^{2+} in Mo_2C [32–35]. There is a certain amount of molybdenum in higher valence on the surface as a result of passivation before the detection of the catalysts. The peaks located at 228.7 eV, 229.9 eV, and 232.6 eV are considered to be originated from $Mo^{\delta+(2<\delta<4)}$, Mo^{4+}, and Mo^{6+}, respectively [36,37]. These peaks ascribed to molybdenum with higher valence are caused by the oxidation of Mo_2C [33,34]. The C 1s spectra were deconvoluted into four peaks, and the peaks centered at 283.3 eV are ascribed to the Mo-C in Mo_2C, which coincides with the XRD results. The other peaks located at 284.6 eV, 286.1 eV, and 288.7 eV are ascribed to C-C, C-O, and C=O, respectively [32]. The emergence of C-C peaks may be caused by polluted carbon, amorphous carbon, and graphitized carbon [38]. Since XPS spectra were obtained under the same experimental conditions simultaneously, the impact of contaminant C in the deconvolution of the C 1s peak and related discussions can be considered as a systematic error.

The surface content of all elements on different catalysts was calculated with the peak area and sensitivity factor, and the results are shown in Table S2. It is found that the surface C contents increase with the increase in the carbon atoms of the used diamines, while those of Mo and O decrease. The above results are consistent with those obtained from element analysis, wherein the Mo_2C-12 owns the highest content of C (52.1%) but with the lowest content of Mo (24.6%). On the one hand, more carbon in the precursor is conducive to the reduction of molybdenum oxides. On the other hand, excessive carbon would cover the surface of the catalyst, which is in accordance with the results of TEM that amorphous carbon was detected.

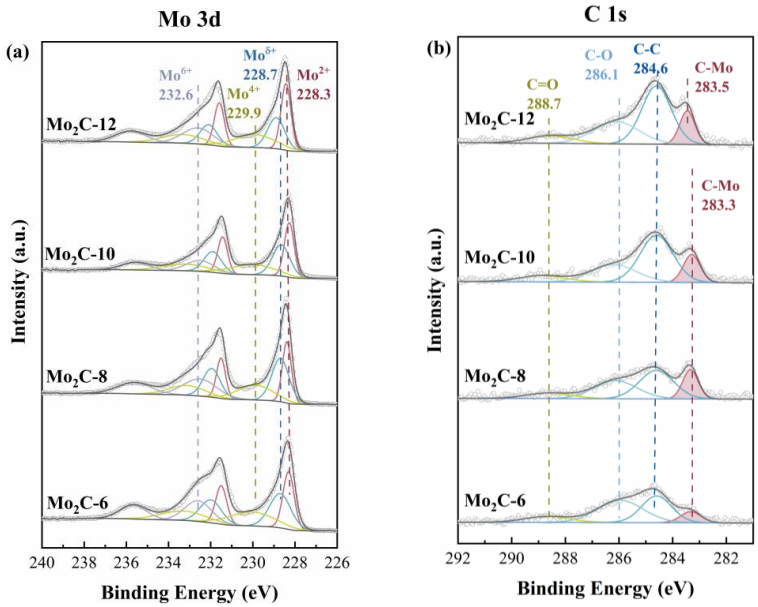

Figure 6. XPS spectra of Mo_2C catalysts (**a**) Mo 3d and (**b**) C 1s.

2.1.6. Raman Result

In order to investigate the existence of different forms of carbon in these Mo_2C catalysts, Raman spectroscopy experiments were conducted. As shown in Figure 7, the scattering peaks located at 1331 cm^{-1} (D-bond) and 1575 cm^{-1} (G-bond) refer to amorphous carbon and graphite carbon, respectively [31,39]. Among them, the intensities of these peaks over Mo_2C-6 are rather low. However, as the carbon number of diamines in the precursors increases, both the intensities of D-bonds and G-bonds gradually strengthen, which is consistent with the results of TEM, elemental analysis, and XPS. The intensity of G-bond/D-bond (I_G/I_D) on catalysts Mo_2C-8, Mo_2C-10, and Mo_2C-12 values were 1.16, 0.94, and 0.94, respectively, implying that higher carbon numbers of diamines in the precursor are favorable for keeping higher carbon contents, and more amorphous carbon was formed on the catalyst.

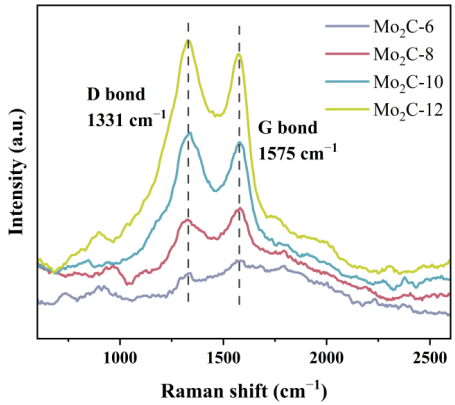

Figure 7. Raman spectra of Mo_2C catalysts.

2.2. The Conversion of Palmitic Acid over Molybdenum Carbide Catalysts

The catalytic performances of different catalysts were evaluated by hydrogenating palmitic acid. The presented activity results were repeated three times, as shown in Figure 8a. It is found that all the catalysts are capable of achieving the complete conversion of palmitic acid after reacting for 8 h. However, both the yield and selectivity of hexadecane increased with the increase in carbon number in diamine when preparing AMO precursor. Among them, the selectivity of hexadecane over Mo_2C-6 was 73.3%, while that on Mo_2C-12 reached the highest 96.6%. Noteworthy, the selectivity of pentadecane on all catalysts was less than 1.5%, which proves that the main deoxygenation pathway for converting palmitic acid over these Mo_2C catalysts is hydrodeoxygenation (HDO) rather than decarbonylation (DCO) or decarboxylation (DCO_2).

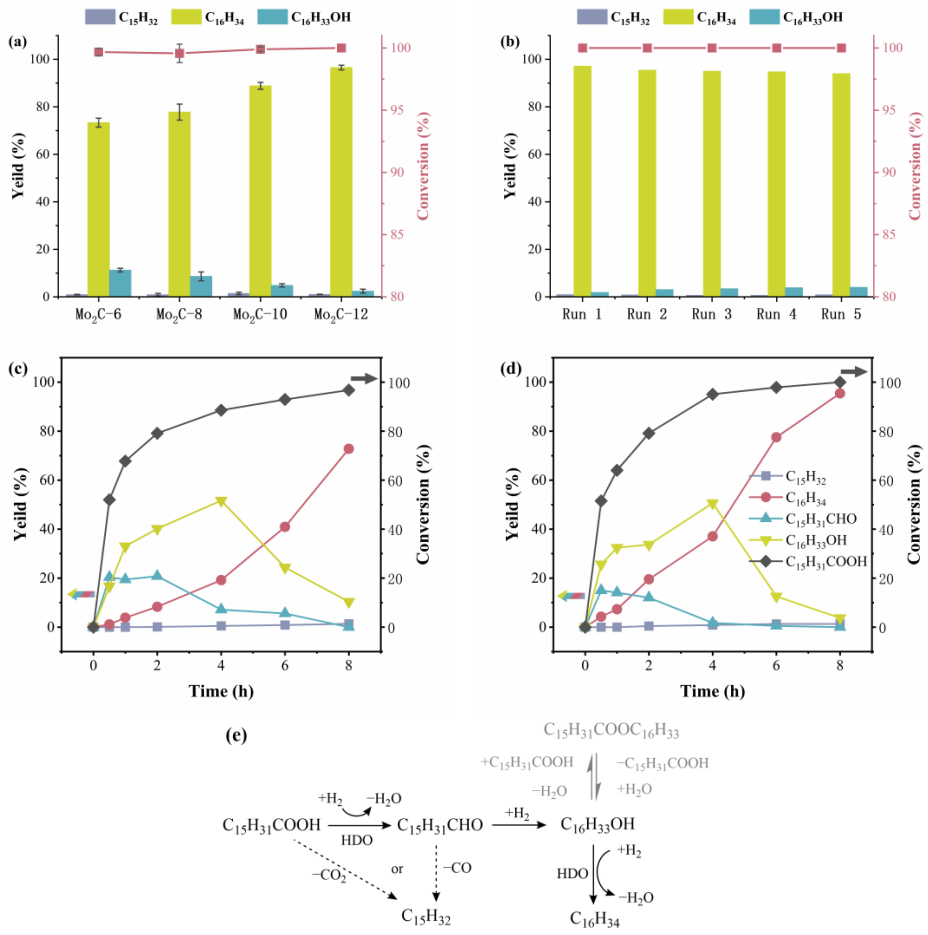

Figure 8. (**a**) The reactivity results for converting palmitic acid over different Mo_2C catalysts. (**b**) The recycling results of Mo_2C-12 catalyst. (**c**) The time-on-stream profile of palmitic acid conversion over Mo_2C-6. (**d**) The time-on-stream profile of palmitic acid conversion over Mo_2C-12. (**e**) Possible reaction pathway in the HDO of palmitic acid via Mo_2C-12 catalyst.

Since the Mo_2C-6 and Mo_2C-12 catalysts exhibited the worst and best catalytic performance, respectively, towards the hydrogenation of palmitic acid, the dynamic changes of products with the prolongation of reaction time were investigated. As shown in Figure 8c,d, the change trends of palmitic acid and all products were analogous on the two catalysts. It can be seen that a certain amount of hexadecaldehyde was generated in the initial stage of reaction. As the reaction time increased, the conversion rate of palmitic acid continued to increase, and the yield of hexadecaldehyde also continued to decrease. After 4 h of reaction, the conversion rate of palmitic acid on Mo_2C-6 and Mo_2C-12 reached 88.6% and 95.1%, respectively, and the yield of hexadecaldehyde decreased significantly. During the reaction

process, the yield of hexadecanol first increased and then decreased, the turning point represented at 4 h. Meanwhile, the yield of hexadecane continued to increase, indicating that hexadecaldehyde and hexadecanol are important intermediates for the hydrogenation and deoxygenation of palmitic acid to produce hexadecane. It can be inferred that the conversion pathway of palmitic acid on Mo_2C-12 catalyst is hydrogenation deoxygenation. It should be noted that the summation yield of all products is different from the conversion rate. This is probably due to the esterification reaction between palmitic acid and the intermediate product hexadecanol, resulting in the formation of palmityl palmitate [40,41], which is undetected. As shown in Figure 8e, palmitic acid was converted to hexadecaldehyde firstly, and then hexadecanol and hexadecane were further formed. There might be a reversible esterification reaction between hexadecanol and palmitic acid to produce palmityl palmitate. Palmitic acid can be completely converted after 8 h of reaction. It is clear that the yield of pentane is very low during the entire reaction process, which further confirms that the main deoxygenation pathway of palmitic acid over the Mo_2C catalysts is HDO, which is similar to the result reported by Du and Peroni et al. [16,42]. It is notable that during the initial stage of the reaction, the conversion rates of palmitic acid on the two catalysts were close, but more hexadecanol was produced in the reaction using Mo_2C-12. Since hexadecanol is the product obtained by further hydrogenation of hexadecaldehyde, Mo_2C-12 is considered to be able to convert the reaction intermediates faster and thus have better catalytic effects.

The reusability of catalysts is vital for recycling. Therefore, the lifetime tests were carried out, and the corresponding results are shown in Figure 8b. It is shown that both the conversion rate of palmitic acid and the selectivity of hexadecane remain stable without obvious change after consecutive runs for five times. For the fifth run, the conversion and hexadecane yield are still as high as 100% and 94.0%, respectively, showing no significant decrease compared to the fresh catalyst. Moreover, the XRD pattern of the catalysts used for five times all exhibit no obvious change compared to the fresh one, as shown in Figure S2. Altogether, the available experimental data indicate that Mo_2C-12 exhibits outstanding catalytic stability with a slight decrease in catalytic activity, particularly in the conversion of palmitic acid to hexadecane.

Compared with other reports for converting fatty acids (as listed in Table 2), the catalytic performance of Mo_2C-12 catalyst can accomplish the complete conversion of palmitic acid, and a high yield of alkanes was obtained, which is close to the results obtained over precious metal catalysts or other types of catalysts.

Table 2. The activity performance over various catalysts in the conversion of fatty acids.

Catalysts	Raw Material	Reaction Conditions	Activity Performance	Ref.
Pd/C	Stearic acid	Batch reactor, T = 360 °C, P = 1.7 MPa (5% H_2/He), t = 6 h Rea/Cat(wt/wt) = 20	60% conversion, 90% alkanes selectivity	[43]
Ru/C	Stearic acid	Batch reactor, T = 330 °C, P = 1 MPa N_2, t = 12.5 h, Rea/Cat(wt/wt) = 10	100% conversion, 90% alkanes selectivity	[14]
Ni/P-MIL-101	Palmitic acid	Batch reactor, T = 400 °C, P = 3 MPa H_2, t = 3 h, Rea/Cat(wt/wt) = 20	100% conversion, 100% alkanes selectivity	[44]
Ni_2P/SiO_2–γ-Al_2O_3	Methyl palmitate	Trickle-bed reactor, T = 290 °C, P = 3 MPa H_2, H_2/feed = 600 Nm^3/m^3, WHSV = 5 h^{-1}	100% conversion, 99% pentadecane selectivity	[45]
Ni/CeO_2	Palmitic acid	Batch reactor, T = 270 °C, P = 2 MPa H_2, t = 10 h, Rea/Cat(wt/wt) = 5	100% conversion, 94.8% pentadecane selectivity	[46]

Table 2. *Cont.*

Catalysts	Raw Material	Reaction Conditions	Activity Performance	Ref.
Ni-Mo(R)/ZSM-5	Palmitic acid	Batch reactor, T = 300 °C, P = 3.5 MPa H_2, *t* = 4 h, Rea/Cat(wt/wt) = 4	100% conversion, 99% alkanes selectivity	[47]
$Ni/MoO_2@Mo_2CT_x$	Palmitic acid	Batch reactor, T = 280 °C, P = 4 MPa H_2, *t* = 4 h, Rea/Cat(wt/wt) = 5	100% conversion, 97.09 alkanes selectivity	[48]
$Mo_{2.56}CN_{0.50}$	Palmitic acid	Trickle-bed reactor, T = 300 °C, P = 4 MPa H_2, H_2/feed = 600 Nm^3/m^3, WHSV = 50.84 h^{-1}	99.9% conversion, 81.0% pentadecane selectivity	[49]
Ni_3Mo_3N@600	Palmitic acid	Batch reactor, T = 270 °C, P = 2 MPa H_2, *t* = 10 h, Rea/Cat(wt/wt) = 10	100% conversion, 94.3% alkanes selectivity	[50]
Mo_2C-12	Palmitic acid	Batch reactor, T = 275 °C, P = 2 MPa H_2, *t* = 8 h, Rea/Cat(wt/wt) = 5	100% conversion, 96.7% alkanes selectivity	This work

2.3. The Structure–Activity Relationship of Mo_2C Catalysts

All catalysts are directly obtained by thermal decomposition of AMO precursors, and the trend of carbon content in the surface and bulk phase of catalysts is consistent with that in precursors. On the one hand, the higher carbon content in the AMO precursor is beneficial to disperse Mo_2C better during the carbonization process, thus the crystallite size of Mo_2C-12 is the smallest. On the other hand, the surface carbon may also play a role in stabilizing the active phase, which brings excellent reusability to Mo_2C-12. The research of Li et al. [31] prepared Mo_2C@C catalysts for HER through carbonizing organic–octamolybdate crystalline superstructures. They proved that the synergistic interaction between Mo_2C nanoparticles and carbon layers is the primary source of electrocatalytic activity. Wang et al. also found that the synergetic effect of metal and carbon nanotubes leads to the stable activity of Ni^0 [51]. Pores with larger sizes are favorable for adsorbing substrates, transferring intermediates, and desorbing products, especially for large-sized molecules. With the largest pore size, the catalytic performance of Mo_2C-12 may be improved by affecting mass transfer during the reaction. Wang et al. [52] reported that the $NiMoS/Al_2O_3$ catalyst with larger pores (19.2 nm) of Al_2O_3 support was beneficial for the rapid diffusion of products in the pores, thus improving the HDO performance of the catalyst.

3. Materials and Methods

3.1. Materials

Ammonium molybdate tetrahydrate ($(NH_4)_6Mo_7O_{24}{\cdot}4H_2O$, AHM, ≥99.0%), palmitic acid ($C_{15}H_{31}COOH$, ≥99%), and heptane (using as solvent, C_7H_{18}, ≥99.0%) were purchased from Chron Chemical Co. in Chengdu, China. 1,6-Hexanediamine ($C_6H_{18}N_2$, ≥99.0%); 1,8-Diaminooctane ($C_8H_{20}N_2$, 98%); 1,10-Diaminodecane ($C_{10}H_{26}N_2$, ≥98.5%); and 1,12-Diaminododecane ($C_{12}H_{30}N_2$, 97%) were purchased from Adamas Co., Shanghai, China. All the reagents were used directly without further purification. H_2, Ar, and $5\%O_2/N_2$ were all purchased from Chengdu Xuyuan Chemical Co., Chengdu, China.

3.2. Catalysts Preparation

The synthesis method for a series of Mo_2C catalysts was adapted from the literature [24] with some modifications. Firstly, an amine–metal oxide (AMO) composite precursor was formed by mixing AHM and different organic diamines in deionized water, then acid was added to promote dissolution. The added molar amount of AHM and different diamines was kept the same. Typically, 2.47 g (2.00 mmol) AHM was dissolved into

50 mL water, and 3.49 g (30.00 mmol) 1,6-Hexanediamine was then added into the above solution. Subsequently, the solution was heated to 60 °C with constant stirring for 30 min. Then, HNO_3 (1 mol/L) was added to adjust the pH value to about 3; at this time, white precipitates were generated completely. Following this procedure, the mixture was kept being stirred under 60 °C for 4 h. Finally, the precipitates were collected by vacuum filtration and then washed with water and ethanol three times. After drying at 80 °C for 12 h, the above obtained precursors were further tableted and crushed into the size of 40–60 meshes. The Mo_2C catalysts were obtained by heating the precursors under Ar atmosphere, i.e., calcining in a tube furnace under Ar flow (30 mL/min) by the temperature programming procedure, which was maintained from room temperature to 700 °C with a heating rate of 5 °C/min and kept at the final temperature for 2 h. After cooling down to room temperature under Ar flow, the sample was later passivated in 5% O_2/N_2 for 2 h to avoid rapid oxidation or spontaneous combustion upon contact with air.

3.3. Catalytic Activity Test

Reactivity evaluation experiments were conducted by selecting palmitic acid as the model compound, and they were performed in a 50 mL stainless steel autoclave (Century Senlong MC50, Beijing, China) with a circulating water system and mechanical stirring at 400 rpm. Typically, 0.25 g palmitic acid, 0.1 g catalyst, and 25 mL heptane were added into the reactor. Then, the reactor was sealed and flushed with 2.0 MPa N_2 three times to replace the air, and then 2.0 MPa H_2 was purged to replace N_2 three times, as well. Finally, 2.0 MPa H_2 was retained in the reactor. Afterward, the reactor was heated to the specified temperature and timed. Once the reaction was completed, the reactor was forced to cool under ice bath, and the pressure was subsequently released. Later, the reaction mixture was taken out, and the catalyst and reaction solution were separated for further analysis. All the activity experiments were repeated three times to ensure accuracy. The used catalyst for the lifetime test was washed with heptane three times and dried at 50 °C in a vacuum oven for 30 min until put for the next run.

The liquid product was quantitatively analyzed by gas chromatography (GC, Panna A91, Zhejiang, China) equipped with a Flame Ionization Detector (FID) and a capillary column (HP-5, 30 m × 0.25 mm × 0.25 μm). The configured sample and internal standard solution were injected into the GC with temperature-programmed heating, and the set procedure was as follows: 70 °C, kept for 3 min, heat to 160 °C at a ramp of 5 °C/min, kept for 3 min, and finally heat to 250 °C at 10 °C/min for 3 min. The conversion and selectivity of each component were calculated by the following equations:

$$\text{Conversion} = (n_0 - n_i)/n_0 \times 100\% \quad (1)$$

n_0 is the initial mole amount of reactant, and n_i is the final mole amount of reactant.

$$\text{Selectivity} = n_p/(n_0 - n_i) \times 100\% \quad (2)$$

n_p is the mole amount of product.

3.4. Catalysts Characterization

X-ray diffraction (XRD) of amine–metal oxide composite precursors was performed on a D2 PHASER (Bruker, Kalkar, Germany). The working conditions were as follows: Cu Kα radiation (λ = 0.1542 nm), step size: 0.04°, scan rate: 5°/min current: 30 kV, and voltage: 10 mA. XRD patterns were recorded from 2 to 60°. XRD of catalysts was performed with an XRD-6100 diffractometer (Shimadzu, Kyoto, Japan) by Cu Kα radiation (λ = 0.1542 nm), with a step size of 0.02° and a scan rate of 5°/min, working current: 40 kV, and voltage: 30 mA. XRD patterns were collected from 10 to 80°. The crystal sizes were calculated using the Scherrer Equation.

X-ray photoelectron spectroscopy (XPS) was carried out with an AXIS Ultra DLD (Kratos, Manchester, Britain). The Al Kα monochromatized line was operated under the

condition of tube power: 144 W, pass energy: 20 eV, and energy step: 0.05 eV. The binding energy was calibrated with C 1 s at 284.6 eV.

Thermogravimetric analysis (TGA) and differential scanning calorimetry (DSC) experiments were conducted on an STA 449 F5 (NETZSCH, Selber, Bavaria, Germany). About 10 mg sample was tested in an Ar flow (30 mL/min), and the temperature was raised from 30 °C to 900 °C at a rate of 5 °C/min.

Raman spectrum was performed with a HORIBA-XploRA PLUS (HORIBA Scientific, Paris, France), with an excitation wavelength of 532 nm and a 1% filter. The spectrum was the average of 10 measurements using a 600 g/mm grating.

Inductively coupled plasma emission spectroscopy (ICP−AES) was performed on an OPTIMA8000 (PerkinElmer, Waltham, MA USA) to measure the molybdenum content in catalysts. All samples were dissolved in aqua regia before analysis, whereas the C, H, and N contents were analyzed using a Vario EL Cub (Elemental, Langenselbold, Hessian, Germany).

Scanning electron microscopy (SEM) images were collected by using a Thermo Scientific Apreo 2C (Thermo Fisher, Waltham, MA, USA). Also, 10 kV accelerating energy was used to obtainthe secondary electron signal

Transmission electron microscopy (TEM) was performed with a Talos F200S (Thermo Fisher, Waltham, MA, USA). The sample was firstly dispersed in anhydrous ethanol and then dissolved sufficiently with ultrasonication. The obtained suspension was dropped through a copper mesh and then dried before being sent to the test chamber.

N_2 isothermal adsorption–desorption experiments were performed on a Micromeritics Tristar II 3020 instrument (Micromeritics, Norcross, GA, USA). The BET equation and BJH method were used to calculate the specific surface area and pore size, respectively.

4. Conclusions

Different AMO precursors were synthesized by using diamines with different carbon chain lengths, which can be used to produce β-Mo_2C and carbon through one-step thermal decomposition. During the heating process, the precursors gradually formed α-MoC_{1-x} and then regenerated β-Mo_2C. By changing the carbon number of diamines in the precursors, the bulk and surface carbon content of the catalysts can be adjusted, which can also affect the morphology, structural properties, and crystallite size of the catalysts, thereby affecting their performance in palmitic acid hydrogenation and deoxidation.

When using 1,12-diaminododecane to prepare precursors, Mo_2C-12 obtained by carbonization has the largest pore size, which is beneficial for the conversion of palmitic acid with larger molecular sizes. Mo_2C-12 also has the highest bulk and surface carbon content, and the generated amorphous carbon may disperse and protect the Mo_2C active phase, resulting in better activity and good stability of Mo_2C-12. On the catalyst, the main conversion pathway of palmitic acid is hydrodeoxygenation.

Supplementary Materials: The following supporting information can be downloaded at: https://www.mdpi.com/article/10.3390/catal14020138/s1, Figure S1. TG curves for AMO-10 and AMO-12 in 20% O_2/N_2 atmosphere; Figure S2. XRD patterns of fresh and used Mo_2C-12 catalyst; Figure S3. (a) The reactivity results for converting palmitic acid over different Mo_2C catalysts and MoO_3. (b) XRD pattern of MoO_3; Table S1. Element contents of AMO-10 and AMO-12; Table S2. Surface contents on Mo_2C catalysts calculated form XPS; Table S3. Surface contents of C and Mo in different chemical states in catalysts.

Author Contributions: Conceptualization, methodology, L.Z., X.D. and C.H.; data curation, formal analysis, writing—original draft, L.Z.; writing—review and editing, visualization, supervision, H.Y. and C.H.; project administration, funding acquisition, C.H. All authors have read and agreed to the published version of the manuscript.

Funding: This work was financially supported by the National Natural Science Foundation of China (No. 21536007), 111 project (No. B17030), and the Fundamental Research Funds for the Central Universities.

Data Availability Statement: Data are contained within the article or Supplementary Materials.

Acknowledgments: We would like to thank the Analytical and Testing Center of Sichuan University for the characterization, and we are grateful to Yunfei Tian for his assistance in the XPS experiments.

Conflicts of Interest: The authors declare no conflicts of interest.

References

1. Shindell, D.; Smith, C.J. Climate and air-quality benefits of a realistic phase-out of fossil fuels. *Nature* **2019**, *573*, 408–411. [CrossRef] [PubMed]
2. Smith, P.; Davis, S.J.; Creutzig, F.; Fuss, S.; Minx, J.; Gabrielle, B.; Kato, E.; Jackson, R.B.; Cowie, A.; Kriegler, E.; et al. Biophysical and economic limits to negative CO_2 emissions. *Nat. Clim. Chang.* **2016**, *6*, 42–50. [CrossRef]
3. Degirmenci, H.; Uludag, A.; Ekici, S.; Hikmet Karakoc, T. Analyzing the hydrogen supply chain for airports: Evaluating environmental impact, cost, sustainability, viability, and safety in various scenarios for implementation. *Energy Convers. Manag.* **2023**, *293*, 117537. [CrossRef]
4. Liu, Y.; Hajj, M.; Bao, Y. Review of robot-based damage assessment for offshore wind turbines. *Renew. Sustain. Energy Rev.* **2022**, *158*, 112187. [CrossRef]
5. Berga, L. The Role of Hydropower in Climate Change Mitigation and Adaptation: A Review. *Engineering* **2016**, *2*, 313–318. [CrossRef]
6. Ayachi, S.; He, X.; Yoon, H.J. Solar Thermoelectricity for Power Generation. *Adv. Energy Mater.* **2023**, *13*, 2300937. [CrossRef]
7. Chen, W.-H.; Lee, K.T.; Ong, H.C. Biofuel and Bioenergy Technology. *Energies* **2019**, *12*, 290. [CrossRef]
8. Mukhtar, A.; Saqib, S.; Mubashir, M.; Ullah, S.; Inayat, A.; Mahmood, A.; Ibrahim, M.; Show, P.L. Mitigation of CO_2 emissions by transforming to biofuels: Optimization of biofuels production processes. *Renew. Sustain. Energy Rev.* **2021**, *150*, 111487. [CrossRef]
9. Li, D.; Xin, H.; Du, X.; Hao, X.; Liu, Q.; Hu, C. Recent advances for the production of hydrocarbon biofuel via deoxygenation progress. *Sci. Bull.* **2015**, *60*, 2096–2106. [CrossRef]
10. Xu, J.; Jiang, J.; Zhao, J. Thermochemical conversion of triglycerides for production of drop-in liquid fuels. *Renew. Sustain. Energy Rev.* **2016**, *58*, 331–340. [CrossRef]
11. Ding, S.; Parlett, C.M.A.; Fan, X. Recent developments in multifunctional catalysts for fatty acid hydrodeoxygenation as a route towards biofuels. *Mol. Catal.* **2022**, *523*, 111492. [CrossRef]
12. Kon, K.; Toyao, T.; Onodera, W.; Siddiki, S.M.A.H.; Shimizu, K.-i. Hydrodeoxygenation of Fatty Acids, Triglycerides, and Ketones to Liquid Alkanes by a Pt–MoO_x/TiO_2 Catalyst. *ChemCatChem* **2017**, *9*, 2822–2827. [CrossRef]
13. Phan, D.-P.; Pham, T.M.; Lee, H.; Tran, M.H.; Park, E.D.; Kim, J.; Lee, E.Y. Hydrodeoxygenation of stearic acid over zeolite–MOF composite-supported Pt catalysts. *J. Ind. Eng. Chem.* **2023**, *127*, 590–599. [CrossRef]
14. Zhang, J.; Huo, X.; Li, Y.; Strathmann, T.J. Catalytic Hydrothermal Decarboxylation and Cracking of Fatty Acids and Lipids over Ru/C. *ACS Sustain. Chem. Eng.* **2019**, *7*, 14400–14410. [CrossRef]
15. Deng, Y.; Ge, Y.; Xu, M.; Yu, Q.; Xiao, D.; Yao, S.; Ma, D. Molybdenum Carbide: Controlling the Geometric and Electronic Structure of Noble Metals for the Activation of O–H and C–H Bonds. *Acc. Chem. Res.* **2019**, *52*, 3372–3383. [CrossRef]
16. Du, X.; Liu, J.; Li, D.; Xin, H.; Lei, X.; Zhang, R.; Zhou, L.; Yang, H.; Zeng, Y.; Zhang, H.; et al. Structural and electronic effects boosting Ni-doped Mo_2C catalyst toward high-efficiency C-O/C-C bonds cleavage. *J. Energy Chem.* **2022**, *75*, 109–116. [CrossRef]
17. Lin, Z.; Wan, W.; Yao, S.; Chen, J.G. Cobalt-modified molybdenum carbide as a selective catalyst for hydrodeoxygenation of furfural. *Appl. Catal. B Environ.* **2018**, *233*, 160–166. [CrossRef]
18. Sosa, L.F.; de Souza, P.M.; Rafael, R.A.; Wojcieszak, R.; Briois, V.; Francisco, L.R.; Rabelo-Neto, R.C.; Marceau, E.; Paul, S.; Toniolo, F.S.; et al. Study of the performance of SiO_2-supported Mo_2C and metal-promoted Mo_2C catalysts for the hydrodeoxygenation of m-cresol. *Appl. Catal. B Environ.* **2023**, *331*, 122720. [CrossRef]
19. Chang, Z.; Duan, P.; Xu, Y. Catalytic hydropyrolysis of microalgae: Influence of operating variables on the formation and composition of bio-oil. *Bioresour. Technol.* **2015**, *184*, 349–354. [CrossRef] [PubMed]
20. Xiao, T.; York, A.P.E.; Coleman, K.S.; Claridge, J.B.; Sloan, J.; Charnock, J.; Green, M.L.H. Effect of carburising agent on the structure of molybdenum carbides. *J. Mater. Chem.* **2001**, *11*, 3094–3098. [CrossRef]
21. Galashev, A.Y. Greenhouse effect of clusterization of CO_2 and CH_4 with atmospheric moisture. *Environ. Chem. Lett.* **2011**, *9*, 37–41. [CrossRef]
22. Deng, S.; Shi, X.; Zhao, Y.; Wang, C.; Wu, J.; Yao, X. Catalytic Mo_2C decorated N-doped honeycomb-like carbon network for high stable lithium-sulfur batteries. *Chem. Eng. J.* **2022**, *433*, 133683. [CrossRef]
23. Wan, C.; Regmi, Y.N.; Leonard, B.M. Multiple Phases of Molybdenum Carbide as Electrocatalysts for the Hydrogen Evolution Reaction. *Angew. Chem. Int. Ed.* **2014**, *53*, 6407–6410. [CrossRef]
24. Wan, C.; Knight, N.A.; Leonard, B.M. Crystal structure and morphology control of molybdenum carbide nanomaterials synthesized from an amine–metal oxide composite. *Chem. Commun.* **2013**, *49*, 10409–10411. [CrossRef]
25. Lin, H.; Shi, Z.; He, S.; Yu, X.; Wang, S.; Gao, Q.; Tang, Y. Heteronanowires of MoC–Mo_2C as efficient electrocatalysts for hydrogen evolution reaction. *Chem. Sci.* **2016**, *7*, 3399–3405. [CrossRef]
26. Šljukić, B.; Vujković, M.; Amaral, L.; Santos, D.M.F.; Rocha, R.P.; Sequeira, C.A.C.; Figueiredo, J.L. Carbon-supported Mo_2C electrocatalysts for hydrogen evolution reaction. *J. Mater. Chem. A* **2015**, *3*, 15505–15512. [CrossRef]

27. Gao, Q.; Zhang, C.; Xie, S.; Hua, W.; Zhang, Y.; Ren, N.; Xu, H.; Tang, Y. Synthesis of Nanoporous Molybdenum Carbide Nanowires Based on Organic−Inorganic Hybrid Nanocomposites with Sub-Nanometer Periodic Structures. *Chem. Mater.* **2009**, *21*, 5560–5562. [CrossRef]
28. Sarr, B.; Mbaye, A.; Diop, C.A.K.; Melin, F.; Hellwig, P.; Sidibé, M.; Rousselin, Y. Crystal structure of bis (diisopropylammonium) molybdate. *Acta Crystallogr. Sect. E* **2018**, *74*, 1682–1685. [CrossRef] [PubMed]
29. Upreti, S.; Ramanan, A. Structure-Directing Role of Hydrogen-Bonded Dimers of Phenylenediammonium Cations: Supramolecular Assemblies of Octamolybdate-Based Organic−Inorganic Hybrids. *Cryst. Growth Des.* **2005**, *5*, 1837–1843. [CrossRef]
30. Hubbard, D.J.; Johnston, A.R.; Casalongue, H.S.; Sarjeant, A.N.; Norquist, A.J. Synthetic Approaches for Noncentrosymmetric Molybdates. *Inorg. Chem.* **2008**, *47*, 8518–8525. [CrossRef] [PubMed]
31. Li, J.; Zhang, C.; Wu, C.; Liu, Y.; Zhang, X.; Li, X.; Li, Y.; Sun, J.; Su, Z. Defined organic-octamolybdate crystalline superstructures derived Mo_2C@C as efficient hydrogen evolution electrocatalysts. *Chin. Chem. Lett.* **2023**, *volume*, 108782. [CrossRef]
32. Ren, X.; Zhao, J.; Wei, Q.; Ma, Y.; Guo, H.; Liu, Q.; Wang, Y.; Cui, G.; Asiri, A.M.; Li, B.; et al. High-Performance N_2-to-NH_3 Conversion Electrocatalyzed by Mo_2C Nanorod. *ACS Cent. Sci.* **2019**, *5*, 116–121. [CrossRef] [PubMed]
33. Chen, Y.-Y.; Zhang, Y.; Jiang, W.-J.; Zhang, X.; Dai, Z.; Wan, L.-J.; Hu, J.-S. Pomegranate-like N,P-Doped Mo_2C@C Nanospheres as Highly Active Electrocatalysts for Alkaline Hydrogen Evolution. *ACS Nano* **2016**, *10*, 8851–8860. [CrossRef] [PubMed]
34. Fan, X.; Liu, Y.; Peng, Z.; Zhang, Z.; Zhou, H.; Zhang, X.; Yakobson, B.I.; Goddard, W.A., III; Guo, X.; Hauge, R.H.; et al. Atomic H-Induced Mo_2C Hybrid as an Active and Stable Bifunctional Electrocatalyst. *ACS Nano* **2017**, *11*, 384–394. [CrossRef] [PubMed]
35. Murugappan, K.; Anderson, E.M.; Teschner, D.; Jones, T.E.; Skorupska, K.; Román-Leshkov, Y. Operando NAP-XPS unveils differences in MoO_3 and Mo_2C during hydrodeoxygenation. *Nat. Catal.* **2018**, *1*, 960–967. [CrossRef]
36. Wang, J.; Wang, W.; Ji, L.; Czioska, S.; Guo, L.; Chen, Z. Highly Dispersed Mo_2C Nanoparticles Embedded in Ordered Mesoporous Carbon for Efficient Hydrogen Evolution. *ACS Appl. Energy Mater.* **2018**, *1*, 736–743. [CrossRef]
37. Wang, F.; Zhang, W.; Jiang, J.; Xu, J.; Zhai, Q.; Wei, L.; Long, F.; Liu, C.; Liu, P.; Tan, W.; et al. Nitrogen-rich carbon-supported ultrafine MoC nanoparticles for the hydrotreatment of oleic acid into diesel-like hydrocarbons. *Chem. Eng. J.* **2020**, *382*, 122464. [CrossRef]
38. Du, X.; Zhou, K.; Zhou, L.; Lei, X.; Yang, H.; Li, D.; Hu, C. Efficient catalytic conversion of jatropha oil to high grade biofuel on Ni-Mo_2C/MCM-41 catalysts with tuned surface properties. *J. Energy Chem.* **2021**, *61*, 425–435. [CrossRef]
39. Nguyen, T.P.; Choi, K.S.; Kim, S.Y.; Lee, T.H.; Jang, H.W.; Van Le, Q.; Kim, I.T. Strategy for controlling the morphology and work function of W_2C/WS_2 nanoflowers. *J. Alloys Compd.* **2020**, *829*, 154582. [CrossRef]
40. Žula, M.; Grilc, M.; Likozar, B. Mechanistic reaction micro-kinetics-based structure–activity relationships for palmitic acid hydrodeoxygenation over $NiMoS_x$/Al_2O_3 catalysts. *Chem. Eng. J.* **2023**, *467*, 143425. [CrossRef]
41. Hollak, S.A.W.; Gosselink, R.W.; van Es, D.S.; Bitter, J.H. Comparison of Tungsten and Molybdenum Carbide Catalysts for the Hydrodeoxygenation of Oleic Acid. *ACS Catal.* **2013**, *3*, 2837–2844. [CrossRef]
42. Peroni, M.; Lee, I.; Huang, X.; Baráth, E.; Gutiérrez, O.Y.; Lercher, J.A. Deoxygenation of Palmitic Acid on Unsupported Transition-Metal Phosphides. *ACS Catal.* **2017**, *7*, 6331–6341. [CrossRef]
43. Kubičková, I.; Snåre, M.; Eränen, K.; Mäki-Arvela, P.; Murzin, D.Y. Hydrocarbons for diesel fuel via decarboxylation of vegetable oils. *Catal. Today* **2005**, *106*, 197–200. [CrossRef]
44. Chang, H.; Abdulkareem-Alsultan, G.; Taufiq-Yap, Y.H.; Mohd Izham, S.; Sivasangar, S. Development of porous MIL-101 derived catalyst application for green diesel production. *Fuel* **2024**, *355*, 129459. [CrossRef]
45. Shamanaev, I.V.; Deliy, I.V.; Gerasimov, E.Y.; Pakharukova, V.P.; Kodenev, E.G.; Aleksandrov, P.V.; Bukhtiyarova, G.A. Synergetic Effect of Ni_2P/SiO_2 and γ-Al_2O_3 Physical Mixture in Hydrodeoxygenation of Methyl Palmitate. *Catalysts* **2017**, *7*, 329. [CrossRef]
46. Zeng, Y.; Wang, H.; Yang, H.; Juan, C.; Li, D.; Wen, X.; Zhang, F.; Zou, J.-J.; Peng, C.; Hu, C. Ni nanoparticle coupled surface oxygen vacancies for efficient synergistic conversion of palmitic acid into alkanes. *Chin. J. Catal.* **2023**, *47*, 229–242. [CrossRef]
47. Lee, C.-W.; Lin, P.-Y.; Chen, B.-H.; Kukushkin, R.G.; Yakovlev, V.A. Hydrodeoxygenation of palmitic acid over zeolite-supported nickel catalysts. *Catal. Today* **2021**, *379*, 124–131. [CrossRef]
48. Liang, J.; Chen, T.; Liu, J.; Zhang, Q.; Peng, W.; Li, Y.; Zhang, F.; Fan, X. Chemoselective hydrodeoxygenation of palmitic acid to diesel-like hydrocarbons over Ni/MoO_2@Mo_2CT_x catalyst with extraordinary synergic effect. *Chem. Eng. J.* **2020**, *391*, 123472. [CrossRef]
49. Chen, X.; Chen, X.; Li, C.; Liang, C. Engineering the structural formula of N-doped molybdenum carbide nanowires for the deoxygenation of palmitic acid. *Sustain. Energy Fuels* **2020**, *4*, 2370–2379. [CrossRef]
50. Du, X.; Lei, X.; Zhou, L.; Peng, Y.; Zeng, Y.; Yang, H.; Li, D.; Hu, C.; Garcia, H. Bimetallic Ni and Mo Nitride as an Efficient Catalyst for Hydrodeoxygenation of Palmitic Acid. *ACS Catal.* **2022**, *12*, 4333–4343. [CrossRef]
51. Wang, S.; Wang, Y.; Yao, L.; Hu, C. Temperature hysteresis in dry reforming of methane on Ni/SBA-15 catalyst: Low temperature activity originated from the synergy of Ni^0 and carbon nanotubes. *Appl. Catal. B Environ. Energy* **2023**, *333*, 122756. [CrossRef]
52. Wang, W.; Zhang, K.; Yang, Y.; Liu, H.; Qiao, Z.; Luo, H. Synthesis of mesoporous Al_2O_3 with large surface area and large pore diameter by improved precipitation method. *Microporous Mesoporous Mater.* **2014**, *193*, 47–53. [CrossRef]